

The Kilodegree Extremely Little Telescope (KELT): A Small Robotic Telescope for Large-Area Synoptic Surveys

JOSHUA PEPPER,¹ RICHARD W. POGGE,¹ D. L. DEPOY,¹ J. L. MARSHALL,¹ K. Z. STANEK,¹ AMELIA M. STUTZ,²
SHAWN POINDEXTER,¹ ROBERT SIVERD,¹ THOMAS P. O'BRIEN,¹ MARK TRUEBLOOD,³ AND PATRICIA TRUEBLOOD³

Received 2007 May 15; accepted 2007 July 24; published 2007 August 29

ABSTRACT. The Kilodegree Extremely Little Telescope (KELT) project is a survey for planetary transits of bright stars. It consists of a small-aperture, wide-field automated telescope located at Winer Observatory near Sonoita, Arizona. The telescope surveys a set of $26^\circ \times 26^\circ$ fields that together cover about 25% of the northern sky, and targets stars in the range of $8 < V < 10$ mag, searching for transits by close-in Jupiters. This paper describes the system hardware and software and discusses the quality of the observations. We show that KELT is able to achieve the necessary photometric precision to detect planetary transits around solar-type main-sequence stars.

1. INTRODUCTION

The scientific value of planetary transits of bright stars is well known; for a comprehensive review, see Charbonneau et al. (2007). These transits provide the opportunity to study the internal structure of planets (Guillot 2005), their atmospheric composition (Charbonneau et al. 2002), spin-orbit alignment (Gaudi & Winn 2007), and the presence of rings or moons (Barnes & Fortney 2004). Radial velocity (RV) surveys have searched the brightest stars in the sky for planets and are probing increasingly fainter stars. However, even with significant multiplexing, RV surveys are not able to search large numbers of stars fainter than $V \sim 8$ mag. To find planets around fainter stars, transit surveys are more suitable, and a number of such surveys are under way. These surveys typically have wide fields of view and small apertures to simultaneously monitor tens or hundreds of thousands of stars. These surveys have so far discovered six planets transiting bright stars (Alonso et al. 2004; Bakos et al. 2007; Cameron et al. 2007; McCullough et al. 2006; O'Donovan et al. 2006). In order to discover more such scientifically valuable systems, we have begun a survey to discover transiting planets.

The Kilodegree Extremely Little Telescope (KELT) is designed to meet the objectives described in Pepper et al. (2003) for a wide-field, small-aperture survey for planetary transits of bright stars. That paper derives a model for the ability of a given transit survey to detect close-in giant planets (i.e., hot Jupiters) and determines an optimal survey configuration for targeting $8 < V < 10$ mag main-sequence stars. Based on the model of Pepper et al. (2003), we expect to detect roughly four transiting planets with the KELT survey.

The KELT system has two different observing configurations. The primary configuration is a “survey mode” designed for wide area coverage, either in large strips or an all-sky survey, with the goal of covering broad sections of the sky with a large field of view, at a cadence of a few minutes on a nightly basis throughout most of the observing year. This mode implements the primary scientific driver of KELT and gives this telescope a wider field of view and also targets a brighter magnitude range than other transit surveys of its kind. The second configuration is a “campaign mode,” which uses a smaller field of view and is designed to conduct short-duration, intensive observing campaigns on specific fields. In campaign mode, we have undertaken a 74 day campaign toward the Praesepe open cluster.

In this paper, we describe the instrumentation, deployment, and operations of KELT (§ 2); we characterize the performance of the different components and the overall system in the field (§ 3); we show how precise our photometry is (§ 4); and we provide examples of light curves for variable stars and transit-like events (§ 5).

2. KELT SYSTEM OVERVIEW

2.1. Instrument

KELT consists of an optical assembly (CCD detector, medium-format camera lens, and filter) mounted on a robotic telescope mount. A dedicated computer is used to control the telescope, camera, observation scheduling, and data archiving system tasks. One goal in assembling KELT was to use as many off-the-shelf components and software packages as possible to speed the development.

The KELT detector is an Apogee Instruments⁴ API6E thermoelectrically cooled CCD camera. This camera uses the Ko-

¹ Department of Astronomy, Ohio State University, Columbus, OH; pepper@astronomy.ohio-state.edu.

² Department of Astronomy, University of Arizona, Tucson, AZ.

³ Winer Observatory, Sonoita, AZ.

⁴ See <http://www.ccd.com>.

dak KAF-16801E front-side-illuminated CCD with 4096×4096 $9 \mu\text{m}$ pixels (36.88×36.88 mm detector area) and has peak quantum efficiency of $\sim 65\%$ at 600 nm. The AP16E uses a PCI card and cable to control the camera and thermoelectric cooler (TEC). According to the camera specifications and confirmed by laboratory testing, the camera is operated at a conversion gain of $3.6 e^- \text{ADU}^{-1}$ and delivers a measured readout noise of $\sim 15 e^-$. The device is read out at 14 bit resolution at 1.3 MHz, which gives a full-frame readout time of ~ 30 s. The CCD specifications claim a full-well depth of $\sim 100,000 e^-$, but the 14 bit analog-to-digital converter (ADC) saturates at 16,383 ADU ($\sim 59,000 e^-$). The TEC can cool the device to $\sim 30^\circ\text{C}$ below the ambient air temperature. Nominal dark current is $0.1\text{--}0.2 e^- \text{pixel}^{-1} \text{s}^{-1}$ at an operating temperature of -10°C (typical for 20°C ambient air temperature).

We use two different lenses with KELT. For the wide-angle survey mode, we use a Mamiya 645 80 mm f/1.9 medium-format manual-focus lens with a 42 mm aperture. This lens provides a roughly $23'' \text{pixel}^{-1}$ image scale and a $26^\circ \times 26^\circ$ field of view. To provide a narrow-angle campaign mode, we use a Mamiya 645 200 mm f/2.8 APO manual-focus telephoto lens with a 71 mm aperture. This provides a roughly $9.5'' \text{pixel}^{-1}$ image scale and effective $10.8^\circ \times 10.8^\circ$ field of view. Both lenses have some vignetting at the corners, and the image quality declines toward the outer part of the field, so the effective field of view is circular (see §§ 2.5 and 3.3 for details).

To reject the mostly blue background sky without greatly diminishing the sensitivity to stars (which are mostly redder than the night sky), we use a Kodak Wratten No. 8 red-pass filter with a 50% transmission point at ~ 490 nm (the filter looks yellow to the eye), mounted in front of the KELT lens. The calculated response function of the KELT CCD and filter is shown in Figure 1. The transmission function for the Wratten No. 8 filter is taken from the Kodak Photographic Filters Handbook (Kodak 1998), and the quantum efficiency curve for the Kodak KAF-16801E CCD was provided by the Eastman Kodak Company. The effect of atmospheric transmission on this bandpass is estimated for 1.2 air masses at the altitude of Winer Observatory (1515 m), using the Palomar monochromatic extinction coefficients (Hayes & Latham 1975), which are for an altitude of 1700 m. We did not estimate in detail the atmospheric water vapor or O_2 extinction terms, as these are not important for our application. The effective wavelength of the combined filter+CCD response function (excluding atmospheric effects) is 691 nm, with an effective width of 318 nm, computed following the definition of Schneider et al. (1983). This results in an effective bandpass that is equivalent to a very broad *R*-band filter.

The optical assembly (camera+lens+filter) is mounted on a Paramount ME robotic telescope mount manufactured by Software Bisque.⁵ The Paramount is a research-grade German-

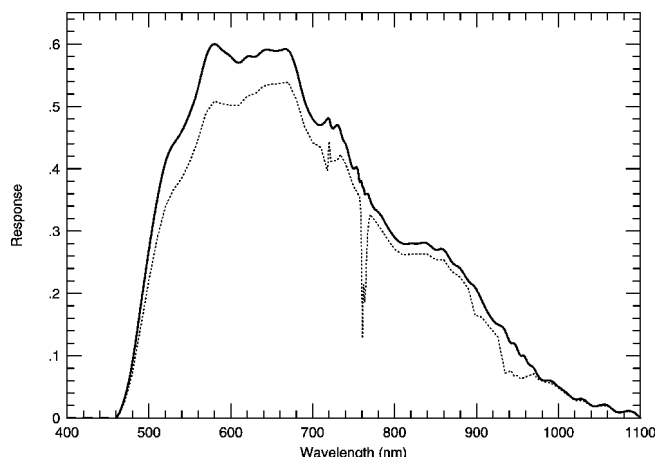


FIG. 1.—Calculated response function of the KELT CCD camera and Kodak No. 8 Wratten filter. The dashed curve is the response function including atmospheric transmission at Winer Observatory for 1.2 air masses. This response function does not include the transmission of the camera lenses.

equatorial mount designed specifically for robotic operation with integrated telescope and camera control. According to the manufacturer's ratings, the periodic tracking error of the mount before correction is $\pm 5''$. That is smaller than the large pixels of the KELT camera and therefore does not affect our observations. The mount can carry an instrument payload of up to 75 kg, more than sufficient for the KELT camera, which weighs approximately 9 kg. The Paramount is installed on a stock 91 cm high steel pier using a stock base adapter plate. The Paramount provides us with a robust, complete mounting solution for our telescope. The optical assembly is mated to the Paramount using a custom mounting bracket that mounts directly on the Paramount's Versa-Plate mounting surface.

The CCD camera and mount are controlled by a PC computer located at the observing site that runs the Windows XP Professional operating system and the Bisque Observatory Software Suite from Software Bisque. There are three main applications that we use for KELT:

1. *TheSky*.—Operates the Paramount ME (pointing and tracking).
2. *CCDSOft*.—CCD camera control software to operate the AP16E camera.
3. *Orchestrate*.—Scripting and automation software to integrate the operation of *TheSky* and *CCDSOft*.

Orchestrate provides a simple scripting interface that lets us control all aspects of a night's observing with a single command script. This software lets us prepare an entire night's observing schedule and upload it to the KELT control computer during the afternoon. A scheduled task on the computer starts up the system at sunset and loads the observing script into *Orchestrate*, after which the system runs unattended for the entire night, weather permitting.

⁵ See <http://www.bisque.com>.

The observing site provides AC power and Internet connectivity. To ensure clean AC power for the KELT telescope and control computer at the observing site (§ 2.2), we use a 1500 VA Powerware 9125 uninterruptible power supply (UPS). This filters the line power and protects the system against surges or brief power outages. The control computer is connected to the Internet through the observing site's gateway, and its internal clock is synchronized with the network time servers at the Kitt Peak National Observatory, using the Dimension 4 network time protocol (NTP) client.⁶ This ensures sufficiently accurate timing for telescope pointing and time-series photometry. Since we observe at few-minute cadences, we can tolerate few-second timing precision, which is easily within the typical performance of Dimension 4 on the available T1 connection.

2.2. Observatory Site

The KELT telescope has been installed at the Irvin M. Winer Memorial Mobile Observatory⁷ near Sonoita, Arizona. Located at north 31°39'53", west 110°36'03", approximately 50 miles southeast of Tucson at an elevation of 4970 feet (1515 m), Winer Observatory has a dedicated observing building with a 25 × 50 foot (7.6 × 15 m) roll-off enclosure, and provides site and maintenance services. Winer currently hosts four robotic telescopes, including KELT. The KELT telescope pier is bolted to the concrete floor, and its control cables are run into a nearby telescope control room that houses the control computer and UPS. Winer also provides Internet access (currently via a dedicated DS/T1 line, but early in the project, the site used a slower ISDN link) that allows us to remotely log in to the control computer via a secure gateway.

The weather conditions at Winer Observatory are roughly as good as comparable sites in southern Arizona; about 60% of all observing time is usable, with half of that time being measurably photometric. Since our point-spread functions (PSFs) are between 2 and 3 pixels, and the pixel scales are 9.5" and 23" (for the 200 and 80 mm lenses, respectively), atmospheric seeing variations (which are on the scale of arc-seconds) are not a factor in our observations.

2.3. Observing Operations

Observations with KELT are carried out each nonclouded night using command scripts for preprogrammed, robotic operation; we do not undertake any remote real-time operations. The nightly observing scripts are created at Ohio State University (OSU) using a script-generation program written in Perl, and then uploaded to Winer Observatory, where they are used by Orchestrator to direct the telescope to observe the specified fields for each night. Each night has a different script, and we

generally upload scripts in 3–4 week batches during the main survey season, or more frequently during pointed-target campaigns.

The suite of software programs we use to control the telescope mount and camera works well, but has several limitations. Most importantly, the Orchestrator scripting package does not provide the built-in ability to program control loops or conditional branching, which is why we use a Perl program to create the Orchestrator scripts we upload to the control computer.

The scripts start the telescope each night, based on the local clock time. On nights when the weather is judged to be good enough for observing, the observatory control computer automatically opens the roof of the observatory at nautical (12°) twilight, and the telescope begins observations on schedule. If the weather is not suitable for observing, on-site personnel abort the command script. If the weather appears good at first but degrades during the night, the observatory computer closes the roof and the personnel abort the script. All data acquired are archived automatically at the end of the night.

When the script is loaded into Orchestrator, it first waits until 1 hr before astronomical (18°) twilight. At that point, the telescope takes five dark images and five bias images, using the same exposure times for the dark frames that will be used later for the night's observations. Once these calibration data are taken, the telescope goes back to sleep until astronomical twilight, at which point it slews to the first target field and begins the nightly observing sequence. Unless the weather turns bad, prompting the roof to close, observations continue until astronomical dawn. At this time, the telescope is slewed to its stowed position, and five dark images and five bias images are acquired, ending observing for the night. (See § 2.5 for a discussion of KELT flat fields.)

We have so far used KELT in two distinct operating modes: campaign mode, using the 200 mm lens, and survey mode, using the 80 mm lens. In campaign mode, the telescope intensively observes a single target field for an entire night. In survey mode, the telescope observes a number of fields that are equally spaced around the sky at 2^h intervals of right ascension centered on a declination of +31°39' (the latitude of Winer).

In campaign mode, the observing script instructs the telescope to wait until the target field is above 2 air masses, and to then observe the field continuously until it sinks below 2 air masses, or until astronomical dawn, whichever happens first. In survey mode, the telescope begins observing after astronomical twilight, tiling between two fields at a time. New fields are observed as they rise above 1.4 air masses. Provisions for Moon avoidance are built into the scripts to prevent observations of any survey field when it is within 45° (two field widths from field center) of the Moon.

An operational complication arises because the KELT mount is a German-equatorial design. This means that fields observed east of the meridian are rotated by 180° relative to fields observed west of the meridian. The practical effect is that we must separately reduce photometry for fields taken in east and

⁶ Version 5.0 from Thinking Man Software, <http://www.thinkman.com/dimension4>.

⁷ See <http://www.winer.org>.

west orientations, especially when we use difference-imaging photometry. To avoid the complication of creating two separate data pipelines to reduce data taken in survey mode, we instead observe only fields in the eastern part of the sky. We lose some observation time due to periods when the Moon is within 45° of all fields in the east above 1.4 air masses, leading to downtime when no field is available that meets the observing criteria. In those situations, the scripts instruct the telescope to pause observing until the next field becomes available. Overall, the loss to Moon avoidance reduces the total amount of data acquired by $\sim 10\%$.

2.4. Data Handling and Archiving

Data acquired by the camera are immediately written to a hard drive in the control computer, logged, and then copied to one of two 250 Gbyte external hard drives attached to the control computer by a USB interface. At the end of the night, all new images are automatically duplicated onto the other external hard drive. During long winter nights, the telescope can take as many as 500–600 images per night, depending on the exposure time, filling the drives every 2 weeks. Normally, however, bad weather and downtime due to Moon avoidance reduce the actual observing rate, so it typically takes 3–4 weeks for both storage drives to reach capacity.

Data quality is monitored daily using automated scripts running on the Windows observing computer at Winer. At the end of the night, a Perl script selects three images from the beginning, middle, and end of the night and uploads them to a computer at OSU. These sample images are analyzed for basic statistics (mean, median, and modal sky value and the mean FWHM of stars measured across the images) and then visually inspected to ensure that the camera and mount are operating correctly.

When the external drives approach full capacity, they are disconnected from the computer. One of the drives is a hardened drive made by Olixir Technologies (their Mobile DataVault), which serves as the transport drive. This drive is shipped via FedEx to the OSU Astronomy Department in Columbus, Ohio, in a cushioned transport box, as bandwidth limitations at Winer Observatory preclude online data transfer. The second drive is a conventional external USB drive without special mobile packaging, made by Maxtor Corporation; this serves as the backup drive and is stored at Winer Observatory. Until the transport drive arrives at OSU and its data have been successfully copied and verified, the backup drive at Winer is stored and left idle. In the event a transport drive arrives damaged, data from the backup drive will be copied to another transport drive and shipped. In the meantime, the removed drives are replaced with two others of each type, and operations continue. At any given time, we have four external disk drives in use: two drives in operation, one in transit, and one stored as a backup. For transferring hundreds of gigabytes of images every few weeks during the prime observing season, this procedure has proven to

be very reliable and efficient. To date, out of dozens of drive shipments, we have lost only two drives to damage in transit, with no loss of data (both arrived damaged at Winer after their data were retrieved and copied at OSU).

When a transport drive arrives at OSU, the drive is connected to our main data storage computer, and all of the images are copied and run through a series of data quality checks. The image files are renamed, replacing the cumbersome default file name created by the CCDSoft application with a name indicating the field observed, the UTC date, and an image number. The images are then analyzed to measure image quality (modal sky and mean FWHM). If the modal sky value is above 800 ADU (due to moonlight, cloud cover, or other ambient light sources), the image is discarded. The cutoff at 800 ADU was determined using 2 months of representative data showing that images compromised by excessive light contamination consistently had sky values above that level and were unsuitable for photometry. The cutoff is high, with many poor images well below the cutoff, but we choose to be conservative about eliminating images early in the reduction process. The images that pass the initial filter on sky values, and the trimmed sections of the bad images, are stored on a multiterabyte RAID storage array at OSU, providing data redundancy and fast access for data reduction and analysis.

2.5. Data Reduction

Here we describe the data reduction process in brief, for the purposes of evaluating the performance of the KELT camera. Detailed descriptions of the reduction process will be included in an upcoming paper on the scientific results of KELT observing campaigns (J. Pepper 2007, in preparation).

The data reduction pipeline consists of three steps. First, we process the images by subtracting dark frames and dividing by a flat field. Second, we identify all the stars in the field and determine their instrumental magnitudes. Third, we obtain the photometry on all images using difference image analysis.

Dark images are created for each night by median-combining 10 dark images: five from the beginning and end of each night. In early testing, we determined that we can treat our dark frames as combined dark+bias. We take bias frames separately to monitor their stability, but do not incorporate them into the reduction process, because the bias has been extremely stable. In cases where dark frames were not taken or there were problems with the images, we use good dark frames from nights bracketing the observations, to create a substitute dark frame. We confirmed that using dark images from nearby nights did not significantly affect the statistics of the subtracted images—our dark images are quite stable from night to night.

The KELT system is challenging to accurately flat-field. For the 200 mm lens, there is a combined decrease in flux of $\sim 18\%$ between the center of the image and the edges, and a decrease of up to $\sim 26\%$ between the center and the corners. For the 80 mm lens, the decrease is $\sim 23\%$ from the center to the edge,

and $\sim 35\%$ from the center to the corners. Because of the large KELT field of view (10.8° and 26° for the 200 and 80 mm lenses, respectively), twilight flats are not useful for flat-fielding, since the twilight sky is not uniform on those scales. Dome flats using a diffuse screen produced reasonable results with high signal-to-noise ratio. The flats are sufficiently repeatable that we do not need to regularly take dome flats. For relative photometry, the dome flats work adequately, and we are able to absolutely flat-field our images to $\sim 5\%$ accuracy.

Once images have been dark-subtracted and flat-fielded, we can then create catalogs of images and measure the brightnesses of stars on the images. This photometric analysis is done in two basic steps. The first is to create a high-quality reference image for a field by combining a few dozen of the best images and then use the DAOPHOT software package (Stetson 1987) to identify all of the stars in the field down to a faint magnitude limit and measure their approximate instrumental magnitudes. (See § 4.1 for the details on how the instrumental magnitudes are calibrated to standard photometry.)

Once a template and DAOPHOT star catalog with baseline instrumental magnitudes have been created, the second step is to process the images with the ISIS image subtraction package (Alard & Lupton 1998; Alard 2000). Our reduction process is similar to that of Hartman et al. (2004). The ISIS package first spatially registers all of the images to align them with the reference image. The reference image is convolved with a kernel for each image and subtracted, creating a difference image. The flux for each star identified on the reference image is then measured on each subtracted image using PSF-fitting photometry. Image subtraction has been shown in limited tests to be equal to or better than other photometric methods for the purposes of transit searches (G. A. Bakos 2006, private communication). In section § 4 below, we provide additional information about the reduction process to obtain relative photometry.

3. INSTRUMENT PERFORMANCE

In this section, we quantify the performance of the KELT system by assessing in turn the telescope mount, the astrometric quality (geometric image quality), the image quality (position-dependent PSF), and photometric sensitivity.

3.1. Telescope Performance

Since the telescope was installed at Winer in 2004 October, the hardware has performed up to specifications. There have been no significant problems with the mount or the control software. The pointing has not been perfect: our fields are so large that minor pointing errors do not significantly affect our scientific results, but during normal operations, the typical intranight drift is $\sim 25'$ in declination and $\sim 9'$ in right ascension. We believe the drift is due to a slight nonperpendicularity between the orientation of the camera and the axis of the mount. While the magnitude of the drift seems large, it represents a

movement of ~ 65 pixels, less than 2% of the size of the field. It does not cause stars to move across large portions of the detector and therefore does not lead to significant changes in the PSFs of individual stars. Since our reduction method utilizes image subtraction, we do lose the ability to take good photometry at the edges of a field. However, because of PSF distortions and other effects (see § 3.3), we already have degraded sensitivity in those regions. Therefore, the loss of coverage and sensitivity due to drift is quite small. Future alignment of the telescope will attempt to reduce or eliminate the drift.

3.2. Astrometric Performance

Measurements of the positions of stars from the Tycho-2 catalog (Høg et al. 2000) are used to determine the conversion between pixel coordinates and celestial coordinates on the KELT images. We use the Astrometrix⁸ package to compute polynomial astrometric solutions for our images, following the procedure described by Calabretta & Greisen (2002). To avoid stars that are saturated on the KELT images, we consider Tycho-2 stars with magnitudes in the range $9.0 \leq V_{\text{Tycho}} \leq 10.0$. From these we select up to 1000 stars per image. A first attempt to compute a global astrometric solution for the entire 4096×4096 image produced large residuals for most of the outer parts of the detector, with discrepancies of many tens of pixels between the predicted and actual positions of Tycho-2 stars. Since our primary goal is to convert pixel coordinates into celestial coordinates on a star-by-star basis, a global solution is not required. We instead divide the image into 25 subimages on a 5×5 grid and perform a separate astrometric solution for each subimage. A third-order polynomial astrometric fit is computed for each subimage, using Astrometrix. The individual subimage fits give much better results, with offsets between predicted and measured positions of catalog stars at the subpixel level, except at the extreme corners of the field. The subframes overlap by a few tens of pixels, and fits to stars common to adjacent subimages are consistent at the arcsecond level. For the 200 mm lens, the typical rms residuals are $\pm 0.8''$, or $<10\%$ of the average pixel size of $\sim 9.5''$. The 80 mm lens has slightly worse rms residuals, $\pm 5''$, or $\sim 20\%$ of a pixel size of $22''$, but is still well within tolerances for our purposes.

Having a good astrometric fit to the images permits a quantitative assessment of the geometric performance of the KELT optics; specifically, variation in pixel size and shape across the field. Since this is a commercial lens with proprietary optical designs, there is no way to determine these properties a priori. This analysis will therefore be useful for anyone contemplating using similar systems, and has implications for the potential use of this setup; for example, such a camera/lens combination cannot be used to construct large-scale image mosaics. Furthermore, while sky subtraction deals with this effect, flat-fielding does not.

⁸ See <http://www.na.astro.it/~radovich/wifix.htm>.

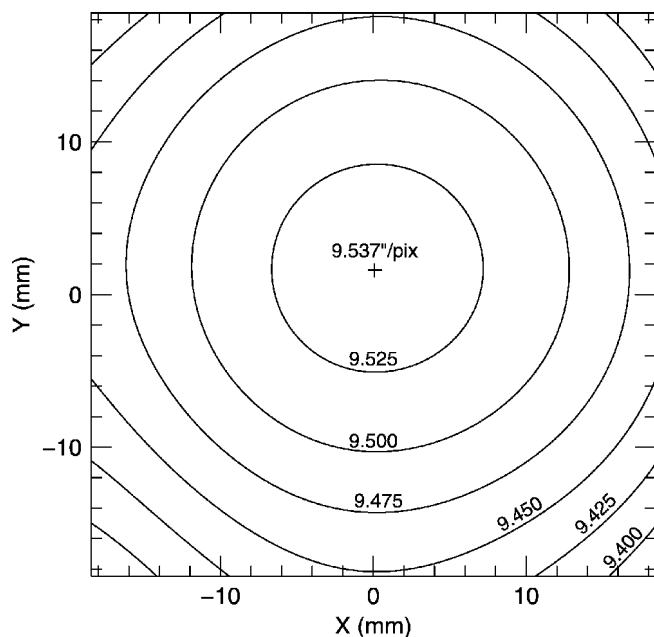


FIG. 2.—Effective pixel scale in arcseconds pixel^{-1} for the KELT 200 mm camera. Contours show curves of constant effective pixel scale. The cross (+) marks the optical center of the field, where the pixel scale is $9.537'' \text{ pixel}^{-1}$.

For the 200 mm lens, the effective pixel size decreases by about 1% from center-to-edge, from $9.537''$ near the center to $9.450''$ at the edges of the field ($\sim 9.40''$ at the corners). Contours of constant effective pixel scale are circular and centered on the intersection of the optical axis of the 200 mm camera lens and the CCD detector, as shown in Figure 2. The square CCD pixels do not perfectly project onto squares on the sky, but slowly distort systematically away from the center, showing the characteristic signature of $\sim 0.5\%$ pincushion distortion, expected from the manufacturer's typical claims for their telephoto lenses. As Figure 3 shows, for the 80 mm lens the effective pixel size decreases by about 3.5% from center to edge, from $23.19''$ near the center to $22.40''$ at the edges of the field (and $\sim 21.8''$ at the corners). This effect is larger than the one seen with the 200 mm lens, consistent with $\sim 2\%$ pincushion distortion in this lens, typical of short focal-length wider angle lenses. Contours of constant effective pixel scale are also circular and centered on the CCD detector.

The effect of the optical distortion is that pixels project onto smaller effective areas on the sky moving radially outward from the center of the CCD, making the sky appear nonflat (center to edge) at the $\sim 1.5\%$ level for the 200 mm lens, and at the $\sim 6\%$ level for the 80 mm lens. There are two effects that act together to decrease the background sky level per pixel as you go radially outward from the center of the image: the decreasing pixel scale, and hence decreasing pixel area on the sky, with radius, and increasing vignetting with radius.

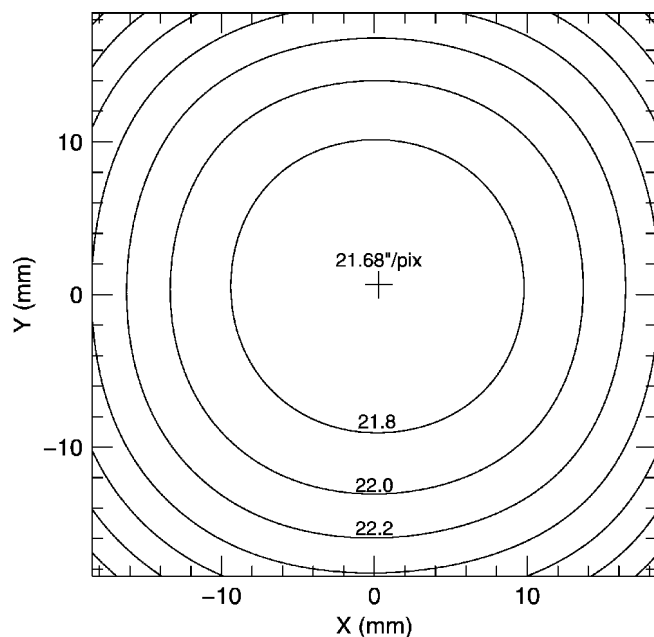


FIG. 3.—Effective pixel scale in arcseconds pixel^{-1} for the KELT 80 mm camera. Contours show curves of constant effective pixel scale. The cross (+) marks the optical center of the field, where the pixel scale is $21.68'' \text{ pixel}^{-1}$.

3.3. Image Quality

As expected for such an optically fast system, the image PSF varies systematically as a function of position. The small physical pixel size ($9 \mu\text{m}$) implies that the lens optics dominate the PSF, and we are insensitive to changes in atmospheric seeing. For both lenses, the systematic patterns in both the image FWHM and more refined measures of image quality (i.e., the 80% encircled energy diameter D_{80}) can be used to quantitatively assess the position-dependent image quality.

For the 200 mm lens, typical image PSFs have FWHMs of ~ 1.8 – 2.9 pixels, and 80% encircled energy diameters of $D_{80} = 4.7$ – 9 pixels. The 80 mm lens has a similar range of FWHMs for stellar image PSFs, and the 80% encircled energy diameters range from $D_{80} = 6$ – 10 pixels. There are significant changes in the detailed PSF shape across each image from the center to the extreme edges of the detector. Figure 4 shows representative stellar PSFs for a 5×5 grid across the CCD for the 200 mm lens. The 80 mm lens shows more pronounced distortions, as shown in Figure 5. Therefore, the 80 mm lens has a roughly 24° diameter effective field of view with reasonably good images and little vignetting, whereas the 200 mm lens works well over most of the CCD detector, except at the extreme corners.

Figures 6 and 7 show maps of the image FWHM as a function of position for the 200 and 80 mm lenses, respectively, derived from measurements of unsaturated, bright field stars in representative images. The most obvious feature in both is the strong

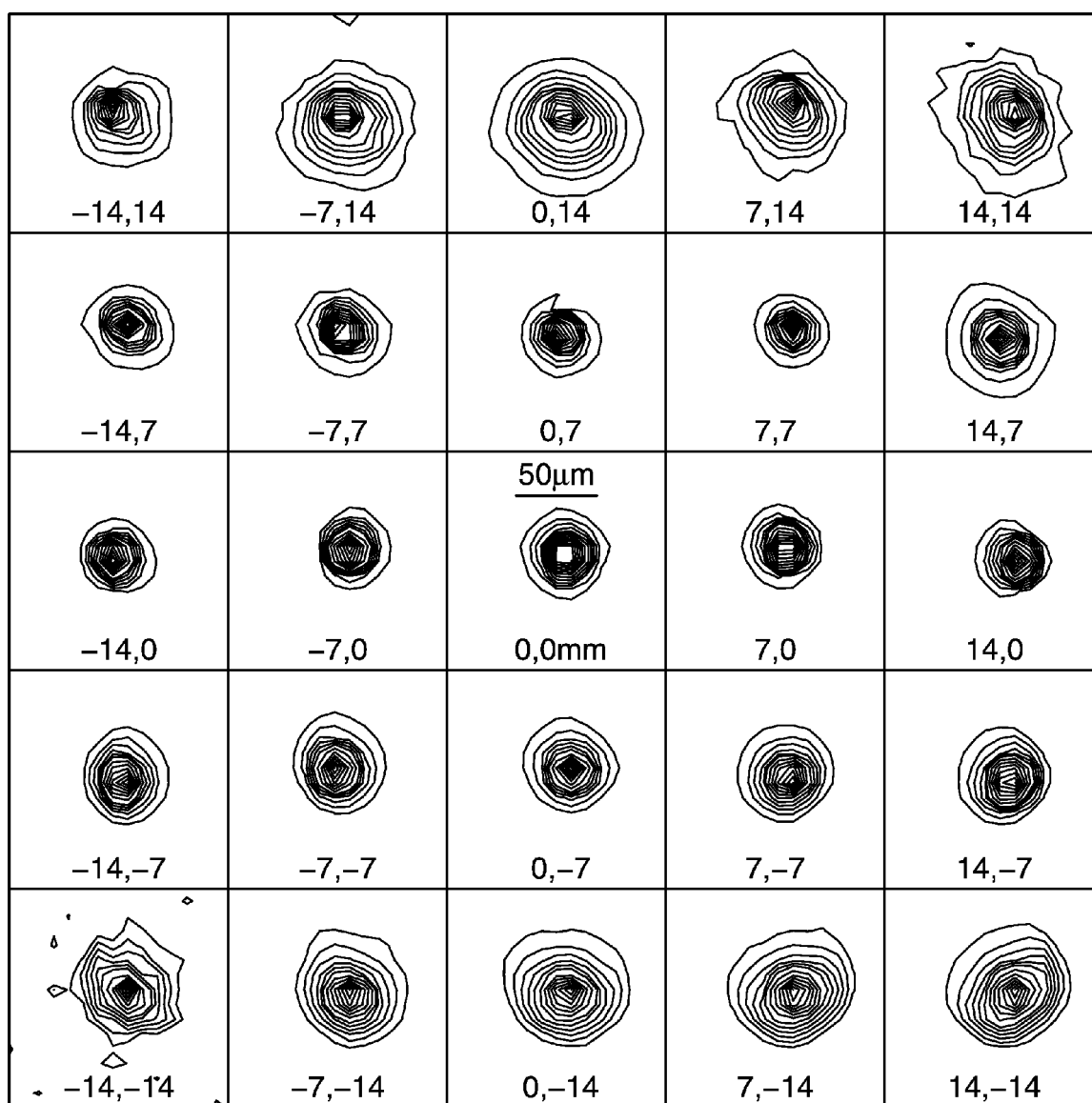


FIG. 4.—Representative stellar PSFs from the 200 mm telephoto lens, shown as intensity contours of bright, unsaturated stars taken with a 5×5 grid pattern on the CCD; the position of the center of each box, relative to the center of the image, is indicated in mm. Each box is 15 pixels (135 μm) on a side. The scale bar in the center panel indicates 50 μm on the detector (5.5 pixels). Contours show levels of (5, 10, 15, 20, 25, 30, 40, 50, 60, 70, 80, 90, 100)% of the peak intensity.

vertical trend in increasing FWHM, with nearly no differences horizontally. Because this is seen with both lenses, which are of very different design, we believe this is because the CCD is tilted relative to the optical axis. Because the lens designs are proprietary, we do not know precisely how much the detector is tilted, nor the origin of the tilt at present. This effect could be due to how the detector is mounted inside the camera, or to the camera/lens mounting plate. This apparent field tilt also affects the maps of the 80% encircled energy diameter D_{80} , shown in Figures 8 and 9.

The 80 mm lens has very stable imaging performance over time. The FWHM and D_{80} maps derived for images of the same field over an 11 month period show no significant changes. However, we have periodically adjusted the focus when working with the telescope, which may cause some discontinuities in the data for the survey images. We will explore such effects in upcoming papers.

Unfortunately, the PSF is not stable across the image over time for the 200 mm lens. While intranight variations in the FWHM maps are quite small, there are significant changes from

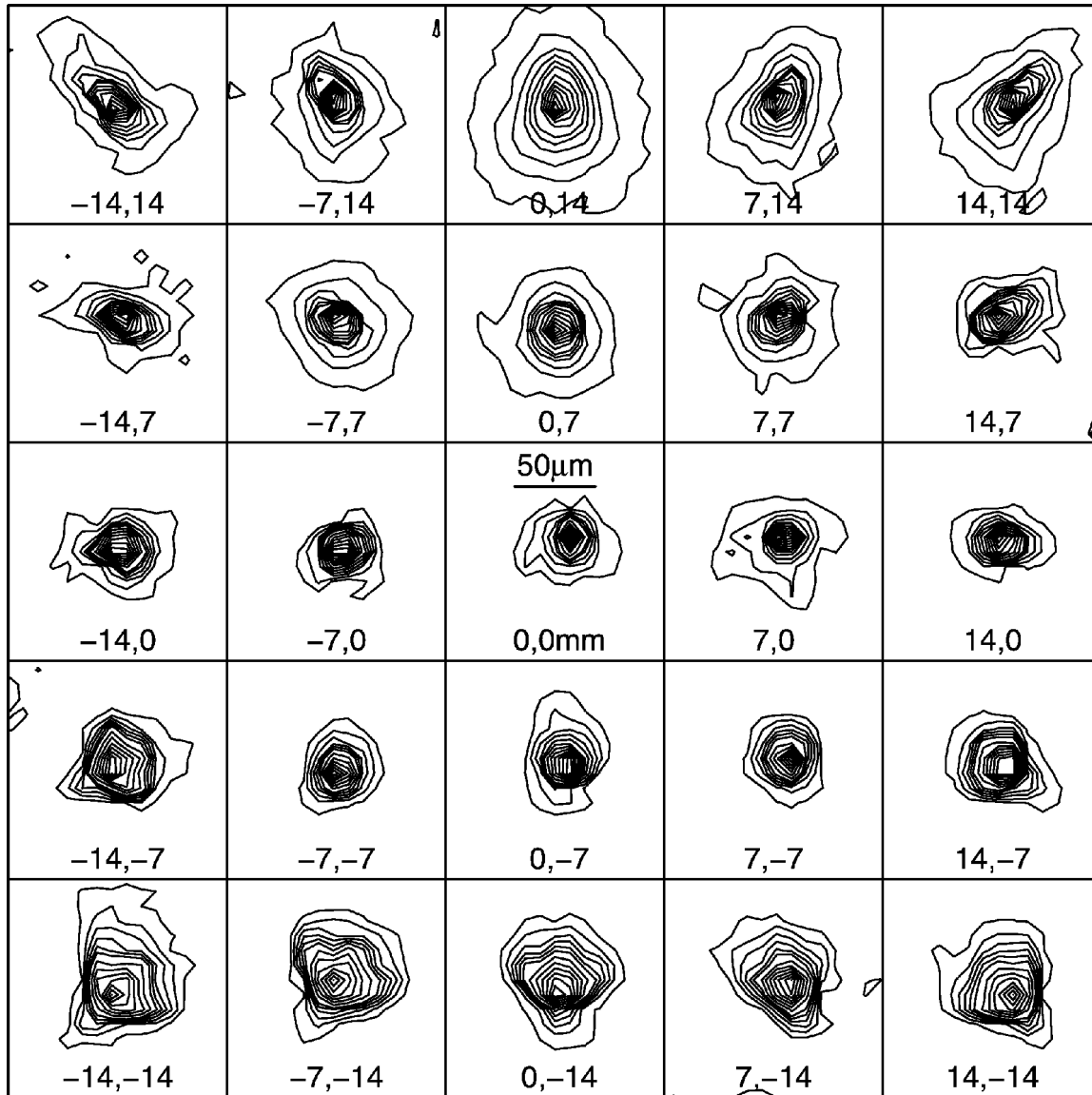


FIG. 5.—Representative stellar PSFs from the 80 mm wide-angle lens, displayed in the same format as in Fig. 4. The images are more severely distorted at the extreme edges of the field than with the 200 mm lens.

night to night that have no apparent correlation with hour angle, CCD temperature, or any other physical or environmental parameter for which we have measurements. The effect of the changes we see is for the region of best FWHM (the base of the trough seen in the FWHM map in Fig. 6) to move vertically on the CCD by many hundreds of pixels. We do not yet know the cause. The main effect is to complicate the difference-imaging reductions of the data. We will discuss these complications and their mitigation in a subsequent paper describing our results for the 200 mm lens Praesepe cluster observing campaign.

3.4. Photometric Sensitivity

Given the nature of the KELT bandpass (see Fig. 1), we calibrate our instrumental magnitudes to the R band. We do so by rescaling our instrumental magnitudes by a constant such that

$$R_K \equiv -2.5 \log (\text{ADU s}^{-1}) + R_{K,0}, \quad (1)$$

where the instrumental ADU s^{-1} is measured using aperture photometry with IRAF, R_K is defined as an approximate KELT R magnitude, and $R_{K,0}$ is the zero point. We find that the R_K

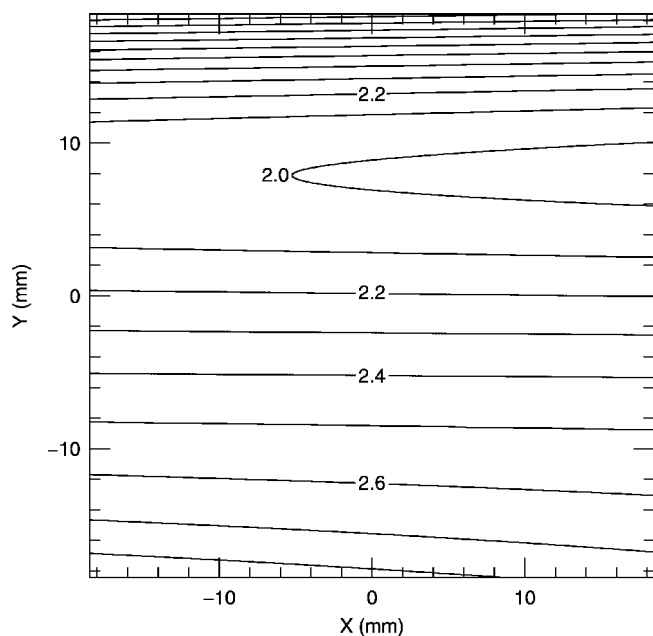


FIG. 6.—Contours of constant FWHM for stellar images in a representative 200 mm lens KELT image, with FWHM given in pixels. Contours are based on a smooth polynomial surface fit to measurements of ~ 1200 bright, unsaturated stars distributed across the image. Contour spacing is every 0.1 pixels, with particular contour level values in pixels as indicated.

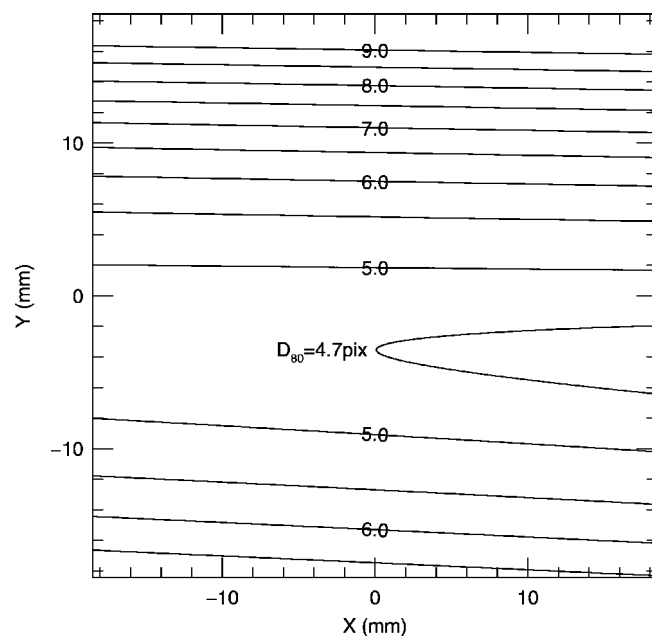


FIG. 8.—Contours of constant 80% encircled energy diameter (D_{80}) in pixels for stellar images in a representative 200 mm lens KELT image. Contours are based on a smooth polynomial surface fit to measurements of ~ 1200 bright, unsaturated stars distributed across the image.

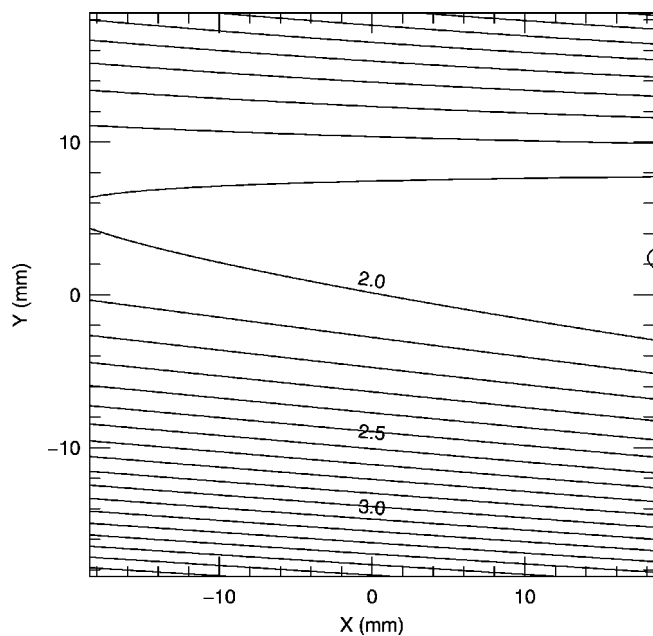


FIG. 7.—Contours of constant FWHM for stellar images in a representative 80 mm lens KELT image, with FWHM given in pixels. Format is the same as in Fig. 6. Contours are based on measurements of ~ 2100 bright, unsaturated stars.

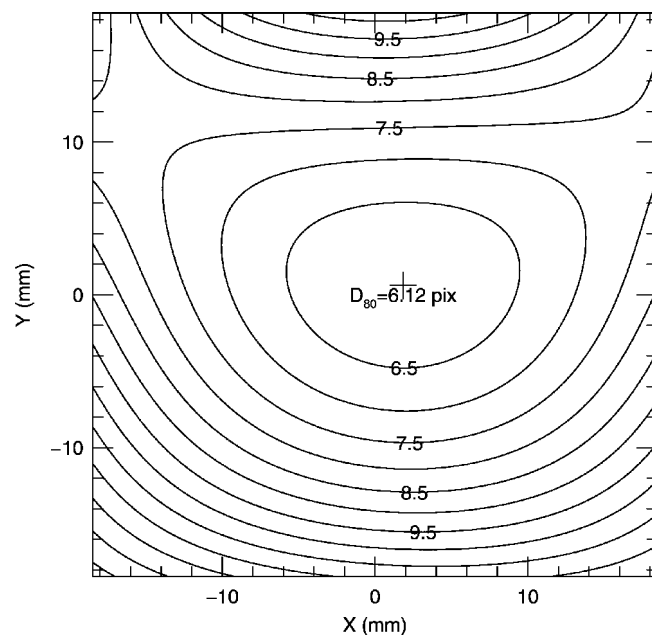


FIG. 9.—Contours of constant 80% encircled energy diameter (D_{80}) in pixels for stellar images in a representative 80 mm lens KELT image. Contours are based on measurements of ~ 2100 bright, unsaturated stars.

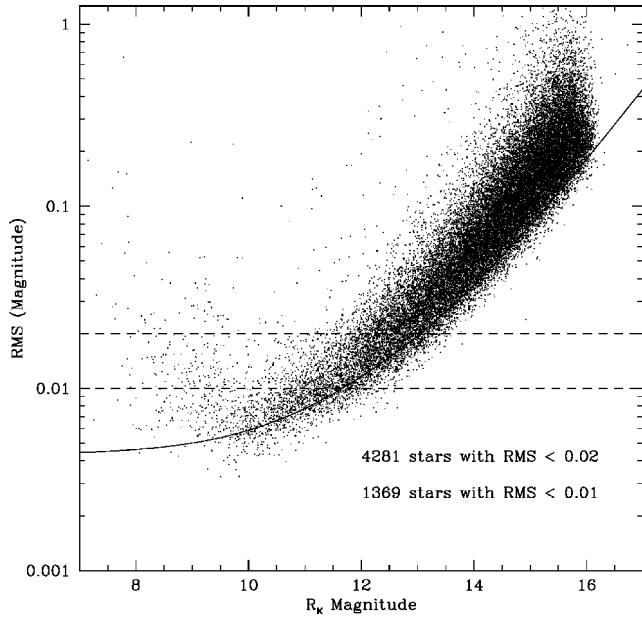


FIG. 10.—rms plot for one night of data from the 200 mm lens. Data are shown for 67,674 stars. The dashed lines show the limits for 1% and 2% rms. The solid line represents a noise model including photon noise and sky noise, along with an rms floor of 0.004 mag.

magnitudes are within a few tenths of a magnitude of standard R band photometry, with the uncertainty dominated by the color term. Since we do not have $V - I$ colors for all our stars, we quote observed magnitudes in R_K , which can be considered equivalent to Johnson R , modulo a color term defined by

$$V = R_K + C_{VI}(V - I), \quad (2)$$

where C_{VI} is the $(V - I)$ color coefficient, and V and I are in the Johnson-Cousins system. Since we do not have previously measured R magnitudes of large numbers of stars in our fields in our magnitude range, we relate R_K to known magnitudes by matching stars from our observations to the *Hipparcos* catalog, selecting only stars with measured V and I colors in *Hipparcos*. We take the mean instrumental magnitude from a set of high-quality images and match the known magnitudes to the mean instrumental magnitudes, using equations (1) and (2).

For the cluster observations with the 200 mm lens, we select 22 calibration stars and measure their instrumental magnitudes on 76 high-quality images, resulting in a magnitude zero point of $R_{K,0} = 16.38 \pm 0.06$ mag, and $C_{VI} = 0.55 \pm 0.2$. For the survey observations with the 80 mm lens, we use 59 stars on 77 images, resulting in a magnitude zero point of $R_{K,0} = 15.15 \pm 0.07$ mag, and $C_{VI} = 0.5 \pm 0.3$. Since the *Hipparcos* stars we use to calibrate our data have $(V - I)$ colors mostly between 0 and 1, we expect our calibrations to be less accurate for redder stars. These measured zero-point uncertainties sug-

gest that the flat-field corrections are good to within $\sim 5\%$ in absolute accuracy.

Tying together the full calibration process, we find that a fiducial $R = 10$ mag star at the field center with $(V - I) = 0$ has a flux of $356 \text{ counts s}^{-1}$ with the 200 mm lens, and $115 \text{ counts s}^{-1}$ with the 80 mm lens. Scaling those numbers by the different aperture sizes of the lenses (71 mm aperture for the 200 mm lens and 42 mm aperture for the 80 mm lens), we find that the 200 mm lens is about 8% more efficient than the 80 mm lens.

4. RELATIVE PHOTOMETRY

KELT was designed primarily for precision time-series relative photometry (see Everett & Howell 2001 for background). The crucial test for our instrument is the ability to obtain long-term light curves with low noise and minimal systematics. A simple test of KELT's photometric performance is to examine the rms of the magnitudes of an ensemble of light curves as a function of magnitude. We apply the ISIS image subtraction package to samples of our data to obtain relative photometry, and measure the statistics of the resulting light curves. Our criteria for the ability to detect planetary transits is the presence of substantial numbers of stars for which the rms of the light curves are below the 2% and 1% levels.

4.1. Difference Imaging Performance

The instrumental magnitudes for the KELT light curves are produced through a combination of ISIS and DAOPHOT photometry. This process involves some careful conversion between DAOPHOT and ISIS flux measurements (see Appendix B of Hartman et al. 2004 for the details of the conversion). First, we create a reference image by combining a number of high-quality images. DAOPHOT measures the instrumental magnitude of the stars on the reference image $m_i(\text{ref})$ based on PSF-fitting photometry, with the magnitude of each star i calculated from the flux by $m_i(\text{ref}) \equiv 25 - 2.5 \log(f_i(\text{ref})) + C_{ap}$, where f_i is the flux measured by DAOPHOT and C_{ap} is an aperture correction to ensure that $m_i(\text{ref}) = 25 - 2.5 \log(c_i)$, where c_i is the counts per second from the star in ADU. ISIS then creates an ensemble of subtracted images for the whole data set, using the reference. To derive the full light curve, ISIS fits a PSF for each star on each subtracted image j , to obtain a flux $f_i(j)$. The DAOPHOT-reported instrumental magnitudes for the reference images serve as the magnitude baseline for the conversion of ISIS fluxes to magnitudes, where the magnitude of the i th star on the j th image is $m_i(j) = m_i(\text{ref}) - 2.5 \log(1 - f_i(j)/f_i(\text{ref}))$.

We then calculate the rms variation of all the detected stars in both the Praesepe data set and for a sample of the survey data. Because of the night-to-night variations in the position of the best image quality on the detector with the 200 mm lens, described at the end of § 3.3, we calculate the rms for the Praesepe data from a single night of observations, to better demonstrate the intrinsic instrumental performance. In Figure 10, we

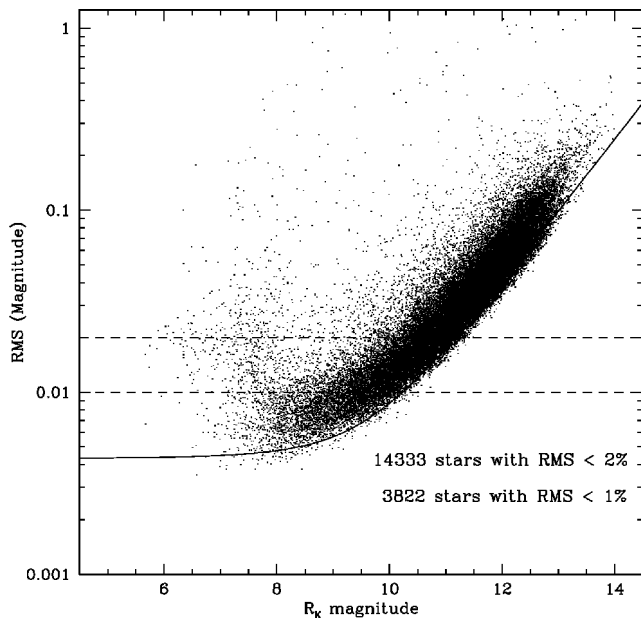


FIG. 11.—rms plot for eight nights of data from the 80 mm lens. Data are shown for 49,376 stars. The dashed lines show the limits for 1% and 2% rms. The solid line represents a noise model including photon noise and sky noise, along with an rms floor of 0.004 mag.

plot the distribution of rms versus R_K magnitude for 67,674 stars on 32 images with 60 s exposures from one night. With this lens and exposure time, we obtain photometry of stars in the magnitude range $R_K = 8$ –16 mag. For stars brighter than about $R_K = 9.5$ mag, systematics begin to dominate the light curves, mostly due to saturation. Out of the 67,674 stars, 4281 have rms < 0.02 mag, and 1369 have rms < 0.01 mag.

We perform the same analysis for one of the regular survey fields observed with the 80 mm lens, using 239 observations over eight nights with 150 s exposures. We obtain photometry on 49,376 stars in the range $R_K = 6$ –14 mag and plot the data in Figure 11. We find 14,333 stars with rms < 0.02 mag, and 3822 stars with rms < 0.01 mag, with systematics dominating for stars brighter than $R_K = 7.5$ mag.

Overall, the rms performance is mostly as expected from Poisson statistics, except at the bright end. The best precision just reaches the theoretical noise limit, with a spread of rms values above that limit due to real-world effects. For the brightest stars in our data, we see a floor in which the rms no longer decreases as the stars get brighter, and instead becomes roughly constant at rms = 0.004 mag. The rms floor is indicative of a fixed-pattern noise component caused by intrapixel sensitivity on the CCD. The Kodak KAF-E series CCDs are two-phase front-side-illuminated devices in which the second poly-gate electrode on each pixel is a transparent gate made of indium-tin-oxide (ITO) to boost the overall quantum efficiency of the device (Meisenzahl et al. 2000). Over much of the wavelength regime of interest for KELT, the ITO material is ~ 2 times more

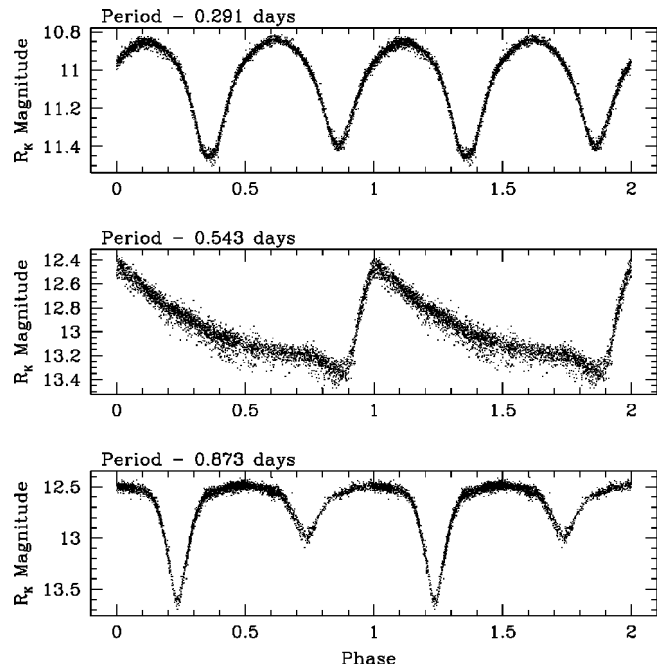


FIG. 12.—Three variable stars discovered with the 200 mm lens in the field of the Praesepe open cluster.

transparent than the regular silicon oxide material used on the first poly-gate. The result is significant pixel substructure in which the quantum efficiency varies stepwise across each 9 μm pixel, which introduces a component of fixed-pattern noise that produces the observed rms floor. We note that more recent models of commercial CCD cameras with the Kodak KAF-16801 detector are using a newer version of this device that incorporate a front-surface microlens array that mitigates the intrapixel step in transmission, but persons contemplating similar systems to our own should be aware of the issue and take it into account.

We do not expect to obtain high-precision photometry for the very brightest stars in our data, but the rms floor is well below the 1% level, and it should not significantly affect our ability to detect transits. We plot noise models in Figures 10 and 11, which include photon noise and sky noise, along with the rms floor. In the future, we will choose a lens focus that makes slightly larger FWHM images, to minimize these effects.

5. REPRESENTATIVE RESULTS

The rms plots shown in Figures 10 and 11 demonstrate that our telescope can obtain precision relative photometry, with large numbers of stars measured at the 1% level. However, simply looking at the rms information does not prove that the data set can yield the consistent quality with low systematics necessary for a transit search. To illustrate that we can fulfill that requirement, we show in Figure 12 the light curves of three sample variable stars we have discovered using the

200 mm lens while observing the field of Praesepe. Even with the night-to-night variations discussed in § 3.3, we are able to achieve the consistent data quality that transit detection requires, and are able to clearly see features in the phased light curves of a few percent or less.

An even better example of our ability to detect transits can be seen in Figure 13. Here we show two objects we detected in our data from the Praesepe field that exhibit transit-like dips in their light curves. These effects can be clearly seen at the level of a few percent. These objects are not planetary: follow-up spectroscopy indicates that the top object is an F star with a transiting M dwarf companion, and the bottom object is a grazing eclipsing binary (D. Latham 2007, private communication). However, they demonstrate that we can confidently detect transit-like behavior at the 1%–2% level with our telescope. A full catalog of the variable stars and transit candidates from the KELT observations of the Praesepe field will appear in a forthcoming paper (J. Pepper 2007, in preparation).

6. SUMMARY AND DISCUSSION

The KELT project has been acquiring data since 2004 October. We observed the field of the Praesepe open cluster with the 200 mm lens for 2 months in early 2005 and have spent the rest of the time using the 80 mm lens for a survey of 13 fields around the northern sky.

The KELT telescope, used in “survey mode” with the 80 mm lens, reflects the design specifications called for in the theoretical paper Pepper et al. (2003). The performance of the telescope as described in this paper provides a real-world evaluation of the potential for this telescope to detect transiting planets. In addition to the light curves and rms plots that show the telescope’s abilities, we find that the total number of photons acquired from a fiducial $V = 10$ mag star over an entire observing run is well above the number assumed in Pepper et al. (2003) with the parameter γ_0 .

This paper has described the KELT instrumentation and performance, with both the 200 mm lens used for observing clusters and the 80 mm lens used for conducting the all-sky survey. It is the widest-field instrument that is currently being employed to search for transiting planets, and we observe brighter stars than other wide-field surveys. The performance metrics demonstrate that it is capable of detecting signals at the $\sim 1\%$ level needed to detect Jupiter-size planets transiting solar-type stars. Further refinements of our reduction process promise to expand our sensitivity to transits, such as applying detrending algorithms of the sort developed by Tamuz et al. (2005). We also plan to conduct a full analysis of red noise (i.e., temporally

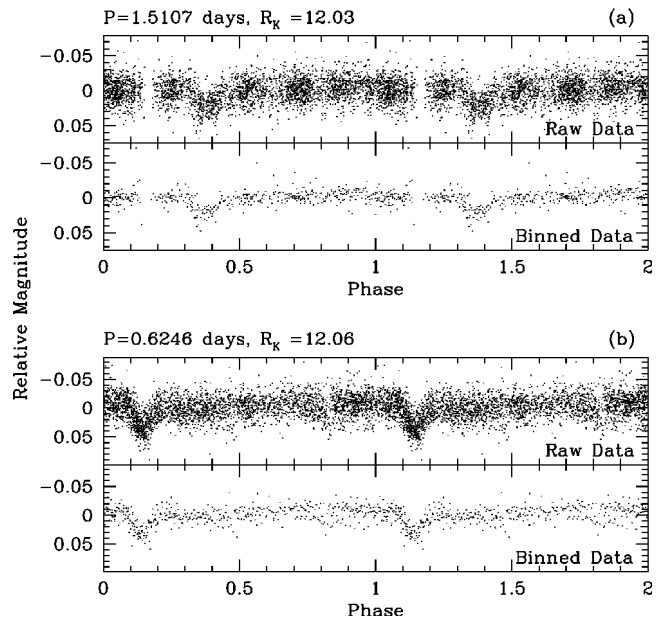


FIG. 13.—Two transit candidates discovered with the 200 mm lens in the field of the Praesepe open cluster. The lower panel of each plot shows the data binned in 10 minute bins. Follow-up spectroscopy indicates that the object in (a) is an F star with a transiting K dwarf companion, and the object in (b) is a grazing eclipsing binary.

correlated systematic noise [see Pont et al. 2006 for a full description]) for all KELT data.

To date, we have detected over 100 previously unknown variable stars in our observations toward Praesepe, and we have identified several light curves with transit-like behavior, of which we show two in Figure 13. Future papers will report on the success in discovering variable stars and searching for planets in Praesepe, along with the full transit search for the all-sky survey.

We would like to thank the many people who have helped with this research, including Scott Gaudi, Andrew Gould, Christopher Burke, and Jerry Mason. We would also like to thank Apogee Instruments and Software Bisque for supplying the camera and mount for the telescope and for excellent service for the hardware. This work was supported by the National Aeronautics and Space Administration under grant No. NNG04GO70G issued through the Origins of Solar Systems program.

REFERENCES

- Alard, C. 2000, *A&AS*, 144, 363
- Alard, C., & Lupton, R. H. 1998, *ApJ*, 503, 325
- Alonso, R., et al. 2004, *ApJ*, 613, L153
- Bakos, G. A., et al. 2007, *ApJ*, 656, 552
- Barnes, J. W., & Fortney, J. J. 2004, *ApJ*, 616, 1193
- Calabretta, M. R., & Greisen, E. W. 2002, *A&A*, 395, 1077

- Cameron, A. C., et al. 2007, *MNRAS*, 375, 951
- Charbonneau, D., Brown, T. M., Burrows, A., & Laughlin, G. 2007, in *Protostars & Planets V*, ed. B. Reipurth, D. Jewitt, & K. Keil (Tucson: University of Arizona Press), 701
- Charbonneau, D., Brown, T. M., Noyes, R. W., & Gilliland, R. L. 2002, *ApJ*, 568, 377
- Everett, M. E., & Howell, S. B. 2001, *PASP*, 113, 1428
- Gaudi, B. S., & Winn, J. N. 2007, *ApJ*, 655, 550
- Guillot, T. 2005, *Ann. Rev. Earth Planet. Sci.*, 33, 493
- Hartman, J. D., Bakos, G., Stanek, K. Z., & Noyes, R. W. 2004, *AJ*, 128, 1761
- Hayes, D. S., & Latham, D. W. 1975, *ApJ*, 197, 593
- Høg, E., et al. 2000, *A&A*, 355, L27
- Kodak 1998, *Kodak Photographic Filters Handbook*, No. B-3 (Rochester: Eastman Kodak)
- McCullough, P. R., et al. 2006, *ApJ*, 648, 1228
- Meisenzahl, E., Chang, W., DesJardin, W., Kosman, S., Shepherd, J., Stevens, E., & Wong, K. 2000, *Proc. SPIE*, 3965, 92
- O'Donovan, F. T., et al. 2006, *ApJ*, 651, L61
- Pepper, J., Gould, A., & Depoy, D. L. 2003, *Acta Astron.*, 53, 213
- Pont, F., Zucker, S., & Queloz, D. 2006, *MNRAS*, 373, 231
- Schneider, D. P., Gunn, J. E., & Hoessel, J. G. 1983, *ApJ*, 264, 337
- Stetson, P. B. 1987, *PASP*, 99, 191
- Tamuz, O., Mazeh, T., & Zucker, S. 2005, *MNRAS*, 356, 1466